ORIGINAL PAPER

A new crack-tip element for the logarithmic stress-singularity of Mode-III cracks in spring interfaces

V. Mantič[1] · A. Vázquez-Sánchez[1] · M. Romero-Laborda[1] · M. Muñoz-Reja[1,3] · S. Jiménez-Alfaro[1,2] · L. Távara[1,3]

Abstract

A new crack-tip finite element able to improve the accuracy of Finite Element Method (FEM) solutions for cracks growing along the Winkler-type spring interfaces between linear elastic adherents is proposed. The spring model for interface fracture, sometimes called Linear-Elastic (perfectly) Brittle Interface Model (LEBIM), can be used, e.g., to analyse fracture of adhesive joints with a thin adhesive layer. Recently an analytical expression for the asymptotic elastic solution with logarithmic stress-singularity at the interface crack tip considering spring-like interface behaviour under fracture Mode III was deduced by some of the authors. Based on this asymptotic solution, a special 5-node triangular crack-tip finite element is developed. The generated special singular shape functions reproduce the radial behaviour of the first main term and shadow terms of the asymptotic solution. This special element implemented in a FEM code written in Matlab has successfully passed various patch tests with spring boundary conditions. The new element allows to model cracks in spring interfaces without the need of using excessively refined FEM meshes, which is one of the current disadvantages in the use of LEBIM when stiff spring interfaces are considered. Numerical tests carried out by *h*-refinement of uniform meshes show that the new singular element consistently provides significantly more accurate results than the standard finite elements, especially for stiff interfaces, which could be relevant for practical applications minimizing computational costs. The new element can also be used to solve other problems with logarithmic stress-singularities.

✉ L. Távara
  ltavara@us.es

  V. Mantič
  mantic@us.es

  A. Vázquez-Sánchez
  avsanchez@us.es

  M. Romero-Laborda
  manromlab@alum.us.es

  M. Muñoz-Reja
  mmunoz@us.es

  S. Jiménez-Alfaro
  sara.jimenez_alfaro@sorbonne-universite.fr

[1] Grupo de Elasticidad y Resistencia de Materiales, Escuela Técnica Superior de Ingeniería, Universidad de Sevilla, Camino de los Descubrimientos s/n, 41092 Sevilla, Spain

[2] Institut Jean Le Rond d'Alembert, Sorbonne Université - CNRS UMR 7190, 4 Place Jussieu, 75000 Paris, France

[3] Escuela Politécnica Superior, Universidad de Sevilla, C/ Virgen de África, 7, 41011 Sevilla, Spain

1 Introduction

Thin adhesive layers in composite laminates or adhesively bonded joints are often modeled as a Winkler-type spring interface [1], given by a continuous distribution of independent linear elastic springs, see [2] for a recent review of this model. The spring interface is also referred to in the literature as the weak interface, linear elastic interface, impedance interface, or Robin interface especially in the mathematical literature. Additionally, in the numerical solution of the unilateral Signorini contact problem, the spring interface is often used to regularise the original contact problem.

Computational analysis and prediction of damage initiation and growth in thin adhesive layers requires a suitable fracture model. An efficient way to model a crack propagating along spring interface, which may represent a thin

adhesive layer, is by means of the Linear-Elastic (perfectly) Brittle Interface Model (LEBIM) [3–7]. It is characterized by a continuous spring-distribution with a linear elastic-brittle law relating the displacement jump across this surface (material separation, in Mode I) and the traction vector acting there. A review of the state of the art of this model can be found in [8]. An accurate calculation of the Energy Release Rate (ERR) is required for modelling crack growth by LEBIM, which depends on the values of the traction vector and the displacement jump (across the interface) at the crack tip. Thus, usually very fine meshes are required at the crack tip when using a numerical approximation [9, 10], especially for stiff interfaces or large cracks.

LEBIM can be considered as a non-smooth limit case of the well-known intrinsic Cohesive Zone Model (CZM) [6, 7, 11–14]. Moreover, results in [15] showed that in some test configurations the LEBIM predictions can better fit experimental results than the predictions by a classical intrinsic CZM. Although LEBIM is a simple and powerful tool, sometimes it may produce inaccurate predictions, associated to a fictitious too compliant interface, much lower than the actual elastic interface stiffness, because the interface stiffness in LEBIM is defined by the interface strength and fracture energy. This drawback can be solved by the application of the Coupled Criterion of Finite Fracture Mechanics (CC-FFM) to spring interface which allows the modelling of (more realistic) very stiff interfaces, because the interface stiffness, strength and fracture energy are independent properties [6, 7, 14, 16–19].

In the past, there have been numerous attempts by researchers to find the first singular terms of the asymptotic series of singular solutions in the crack-tip neighbourhood in non-classical fracture mechanics models such as LEBIM [5, 20–24]. Nevertheless, only very recently a general solution in the form of a complete double asymptotic series for a single material corner with any opening angle and with a spring boundary condition was deduced and analysed for antiplane shear in [25], and particularized for a Mode III crack in spring interface in [26, 27]. Remarkably, in these works it has been shown that there is a logarithmic stress-singularity at the tip of a crack in the spring interface, but with bounded tractions along such interface. The logarithmic stress-singularity is sometimes considered as the weakest singularity that occurs in linear elasticity [28].

The knowledge of these first singular terms is necessary for any efficient computational implementation because they include the terms representing the logarithmic stress-singularity and also the logarithmic singularity of gradient of tractions on the undamaged spring interface. These terms cause difficulties in the numerical solution and lead to potentially high discretisation errors, especially when evaluating the maximum of tractions at the crack tip, if the mesh around the crack tip is not sufficiently fine.

Several approaches have been proposed in the past to increase the accuracy of numerical approximations of non-smooth solutions in the neighbourhood of singular points/edges associated with discontinuities in geometry, material, boundary conditions (e.g., crack tip, re-entrant corner tip, jump in value or type of boundary condition). Some of these methods can almost achieve the accuracy given by the programming language precision, like, e.g., approaches using global shape functions that incorporate singularity functions to enrich the approximation space generated by, e.g., piecewise polynomial shape functions, [29, 30]. However, their general implementation in FEM codes is associated with significant difficulties.

Therefore, following the idea of a very successful quarter-point crack-tip element [31–35] in classical Linear Elastic Fracture Mechanics (LEFM), the main objective of the present article is to develop and test a new crack-tip element for the logarithmic stress-singularities. The aim is to improve the accuracy of FEM solutions predicting propagation of cracks in spring interfaces that appear in modeling, e.g., laminates and joints, and minimize the computational resources used, avoiding the need for an excessive refinement of FEM meshes. Such refinement is currently necessary to achieve a high accuracy of the numerical solution, due to a slow numerical-solution convergence in presence of logarithmic stress-singularities. It is expected that the developed special crack-tip element implemented in a FEM code will allow modeling cracks in spring interfaces without the need of highly refined meshes.

In the present article, the solution of the Laplace equation is used to analyse a linear elastic problem in antiplane shear with a crack under fracture Mode III located in a flat spring interface, focusing on the solution behaviour near the crack tip. Recall that the Laplace equation is relevant for many other kinds of physical problems such as heat transfer, groundwater flow, electrostatics, magnetostatics, etc. [36], the results presented here are therefore directly applicable to all these physical problems.

The solution of an antiplane crack problem in a domain symmetric with respect to a flat spring interface can be decomposed into a symmetric and a skew-symmetric part with respect to the interface plane, similarly as in [26]. The symmetric part of the solution is bounded and smooth near the crack tip, and has zero tractions on the interface plane because the out-of-plane displacements on both sides of the interface are identical, so in simple terms the springs are not stretched. Therefore, we will focus on the skew-symmetric part of the solution. An example of such a skew-symmetric problem with a crack in the spring interface located in the xz-plane is shown in Fig. 1, cf. [5]. It will suffice to study the corresponding Boundary Value Problem (BVP) in a half-domain by replacing the spring interface of stiffness k with

Fig. 1 Schematic of a skew-symmetric antiplane problem with a crack of length $2a$ in a spring interface of stiffness k. **a** 3D view and **b** 2D view, with the shaded part representing a subdomain that can be discretized by FEM once the symmetry conditions are applied
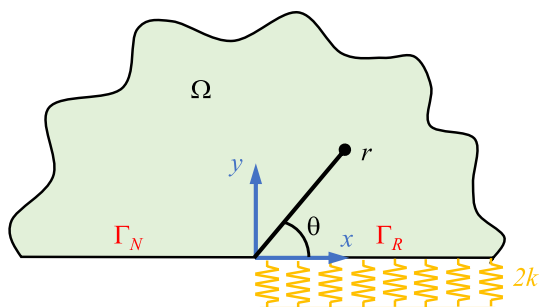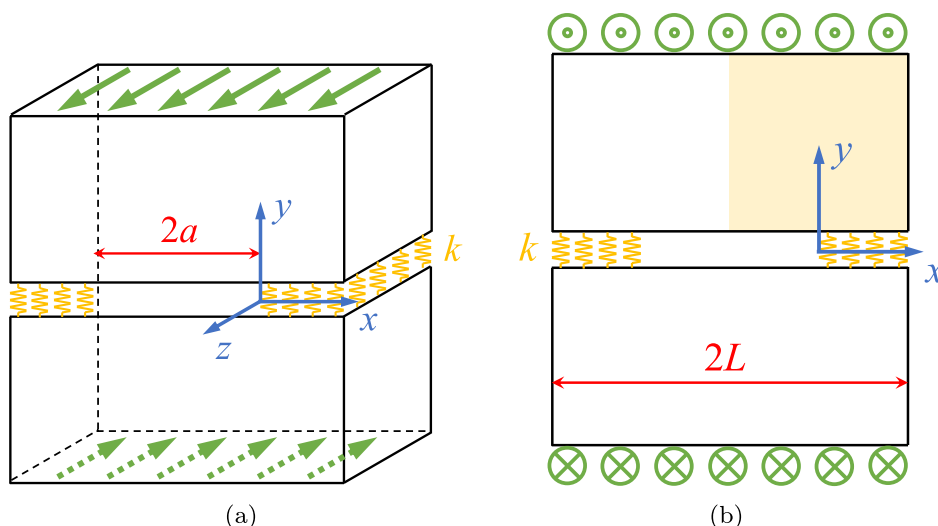

(a)   (b)

Fig. 2 Schematic of the crack-tip neighbourhood in the half domain Ω in which the asymptotic solution is defined

a spring (Robin) boundary condition of double stiffness $2k$, see Figs. 1 and 2.

The article is organized as follows. First, the weak formulation of the Boundary Value Problems (BVPs) with spring boundary condition and the crack-tip solution for a crack in a flat spring interface are introduced in Sects. 2 and 3, respectively. In Sect. 4, the new singular element is introduced, including details of the developed shape functions and resulting stiffness matrix. The results of several numerical test are presented and analysed in Sect. 5. Finally, some conclusions are given in the last section.

2 Weak formulation of a BVP for antiplane shear with Robin boundary condition. FEM approximation

Consider an antiplane shear Boundary Value Problem (BVP), with $u(\mathbf{x}) = u_z(\mathbf{x})$ the out-of-plane displacement, with $\mathbf{x} = (x, y)$, in linear elastic solid represented by its cross-section given by an open 2D domain $\Omega \subset \mathbb{R}^2$, with a Lipschitz boundary $\Gamma = \partial\Omega$, defining the closed domain as

$\overline{\Omega} = \Omega \cup \Gamma$. Dirichlet, Neumann and Robin (spring) boundary conditions are prescribed on the boundary parts Γ_D, Γ_N and Γ_R, respectively. Let $\mathbf{n} = (n_x, n_y)$ define the unit outward normal vector to Γ, $\mu > 0$ being the shear modulus of the linear elastic material in Ω and $2k > 0$ the shear elastic stiffness of the spring distribution on the Robin boundary part Γ_R.

Then, the shear stress component along the boundary is given by

$$\sigma_{nz}(\mathbf{x}) = \mu \frac{\partial u}{\partial n}(\mathbf{x}) = \mu u_{,i}(\mathbf{x}) n_i(\mathbf{x}), \qquad i = 1, 2, \quad \mathbf{x} \in \Gamma. \tag{1}$$

The homogeneous Robin boundary condition, also called spring boundary condition, is defined as

$$\sigma_{nz}(\mathbf{x}) + 2k u(\mathbf{x}) = 0, \qquad \mathbf{x} \in \Gamma_R, \tag{2}$$

or in terms of displacement only

$$\mu \frac{\partial u}{\partial n}(\mathbf{x}) + 2k u(\mathbf{x}) = 0, \qquad \mathbf{x} \in \Gamma_R. \tag{3}$$

Then, the mathematical formulation of the considered BVP for the displacement $u(\mathbf{x})$ can be written as, cf. [37, 38],

$$\mu \Delta u(\mathbf{x}) + f(\mathbf{x}) = 0, \qquad\qquad \mathbf{x} \in \Omega, \tag{4}$$
$$u(\mathbf{x}) = \bar{u}(\mathbf{x}), \qquad\qquad \mathbf{x} \in \Gamma_D, \tag{5}$$
$$\mu \frac{\partial u}{\partial n}(\mathbf{x}) = \bar{\tau}(\mathbf{x}), \qquad\qquad \mathbf{x} \in \Gamma_N, \tag{6}$$
$$\mu \frac{\partial u}{\partial n}(\mathbf{x}) + 2k u(\mathbf{x}) = 0, \qquad\qquad \mathbf{x} \in \Gamma_R, \tag{7}$$

where $f(\mathbf{x})$ is the body force in the z-direction, and $\bar{u}(\mathbf{x})$ and $\bar{\tau}(\mathbf{x})$ are the prescribed displacement and shear stress component on the boundary parts Γ_D and Γ_N, respectively.

By applying the divergence theorem for two displacement fields: $u(\mathbf{x})$, the solution of the above BVP, and $v(\mathbf{x})$, an auxiliary field, both defined in Ω, we get

$$\int_\Omega \mu u_{,i} v_{,i} d\Omega = -\int_\Omega \mu u_{,ii} v d\Omega + \int_\Gamma \mu u_{,i} n_i v d\Gamma. \quad (8)$$

Consider that the auxiliary displacement field vanishes on Γ_D, i.e.

$$v(\mathbf{x}) = 0 \quad \text{for} \quad \mathbf{x} \in \Gamma_D. \quad (9)$$

Then, by applying the definition of the BVP, we get the following weak formulation, which should be verified for any such v

$$\int_\Omega \mu u_{,i} v_{,i} d\Omega + \int_{\Gamma_R} 2kuv d\Gamma = \int_\Omega f v d\Omega$$
$$+ \int_{\Gamma_N} \bar{\tau} v d\Gamma, \quad \forall v, u(\mathbf{x}) = \bar{u}(\mathbf{x}), \quad \mathbf{x} \in \Gamma_D. \quad (10)$$

Consider a discretization of Ω by a triangular finite element mesh, $\overline{\Omega} = \cup_{n=1}^{N_e} \overline{\Omega}_n,$[1] with N nodes $\mathbf{x}_n$ ($n = 1, \ldots, N$), and the associated shape functions $\psi_n(\mathbf{x})$. Let the finite element mesh be characterised by a mesh size parameter $h > 0$.

Let the solution $u(\mathbf{x})$ be approximated by a linear combination of these shape functions, called trial function,

$$u(\mathbf{x}) \cong u_h(\mathbf{x}) = \sum_{n=1}^{N} u_n \psi_n(\mathbf{x}) \quad \mathbf{x} \in \Omega. \quad (11)$$

We assume that these shape functions verify the so-called Lagrange property

$$\psi_n(\mathbf{x}_m) = \delta_{nm}. \quad (12)$$

Then, the coefficients of the above linear combination are nodal values of displacement, i.e.

$$u(\mathbf{x}_n) \cong u_n. \quad (13)$$

We prescribe

$$u_n = \bar{u}(\mathbf{x}_n) \quad \text{for} \quad \mathbf{x}_n \in \Gamma_D, \quad (14)$$

defining the set of known nodal values of displacement approximation.

By introducing the approximation of displacement u into the weak formulation, and taking $v(\mathbf{x}) = \psi_m(\mathbf{x})$ as test function, we get the final linear system for the unknown nodal values of displacement

$$\sum_{n=1}^{N} \left[\int_\Omega \mu \psi_{n,i} \psi_{m,i} d\Omega \right] u_n + \sum_{n=1}^{N} \left[\int_{\Gamma_R} 2k\psi_n \psi_m d\Gamma \right] u_n$$
$$= \int_\Omega f \psi_m d\Omega + \int_{\Gamma_N} \bar{\tau} \psi_m d\Gamma, \quad (15)$$
$$m = 1, \ldots, N \quad \text{with} \quad \mathbf{x}_m \notin \Gamma_D.$$

If the body force in Ω and the prescribed shear $\bar{\tau}$ on Γ_N are also approximated by the above shape functions as

$$f(\mathbf{x}) \cong \sum_{n=1}^{N} f_n \psi_n(\mathbf{x}), \quad \mathbf{x} \in \Omega, \quad (16)$$

$$\bar{\tau}(\mathbf{x}) \cong \sum_{n=1}^{N} \bar{\tau}_n \psi_n(\mathbf{x}), \quad \mathbf{x} \in \Gamma_N, \quad (17)$$

then, this linear system takes the following form, suitable for a computational implementation:

$$\sum_{n=1}^{N} \left[\int_\Omega \mu \psi_{n,i} \psi_{m,i} d\Omega \right] u_n + \sum_{n=1}^{N} \left[\int_{\Gamma_R} 2k\psi_n \psi_m d\Gamma \right] u_n$$
$$= \sum_{n=1}^{N} \left[\int_\Omega \psi_n \psi_m d\Omega \right] f_n + \sum_{n=1}^{N} \left[\int_{\Gamma_N} \psi_n \psi_m d\Gamma \right] \bar{\tau}_n,$$
$$m = 1, \ldots, N \quad \text{with} \quad \mathbf{x}_m \notin \Gamma_D. \quad (18)$$

By defining the elements of stiffness matrix and force vector as

$$K_{mn} = \int_\Omega \mu \psi_{n,i} \psi_{m,i} d\Omega + \int_{\Gamma_R} 2k\psi_n \psi_m d\Gamma, \quad (19)$$

$$F_m = \sum_{n=1}^{N} \left[\int_\Omega \psi_n \psi_m d\Omega \right] f_n + \sum_{n=1}^{N} \left[\int_{\Gamma_N} \psi_n \psi_m d\Gamma \right] \bar{\tau}_n, \quad (20)$$

we get the following form of the final system in the matrix notation:

$$K_{mn} u_n = F_m \quad \text{for} \quad m = 1, \ldots, N \quad \text{with} \quad \mathbf{x}_m \notin \Gamma_D. \quad (21)$$

Once the system (21) is solved considering (14), we can compute the stresses $\sigma_{iz}(\mathbf{x})$ ($i = x, y$) by element-wise differentiating the FEM approximation of the displacement field in (11) as

---

[1] $\overline{\Omega}_n$ represents the closure of an open subdomain Ω_n, i.e. the subdomain and its boundary. In this sense, an open subdomain Ω_n does not include its boundary.

$$\sigma_{iz}(\mathbf{x}) = \mu \sum_{n=1}^{N} u_n \psi_{n,i}(\mathbf{x}), \qquad \mathbf{x} \in \bigcup_{m=1}^{N_e} \Omega_m. \tag{22}$$

Recall that such element-wise approximation of stresses is in general discontinuous between elements. Nevertheless, this is a good option to asses the convergence of the finite element solution, in the sense that big jumps of stresses between elements indicate that the stress solution has not converged yet to the exact solution of the problem. There are many options to get a smooth stress solution by the so-called recovered nodal stress values. One of the best and simple technique is Zienkiewicz–Zhu's derivative (stress) patch recovery technique [39].

However, in the case of singular points (e.g., crack tip, jumps in the value or type of the boundary condition), where stresses are discontinuous or singular, the usage of such recovery techniques is not suitable. Its use in general would lead to worse values and fictitious smoothness of the solution.

3 Crack-tip solution for cracks in spring interfaces

According to [26], the study of a boundary value problem (BVP) in a symmetric domain with a crack in the spring (Robin) interface, as shown in Fig. 1, can be basically reduced, by symmetry arguments, to the study of another BVP corresponding to its skew-symmetric part defined in the upper-half domain only, with a suitable spring boundary condition, as shown in Fig. 2.

Thus, the out-of-plane displacement $u(\mathbf{x})$ in the neighbourhood of the crack tip located in a straight spring interface is given by two boundary conditions: *i)* a homogeneous Robin boundary condition ahead of the crack tip on the boundary part Γ_R, where a continuous distribution of linear elastic springs with stiffness $2k$ is considered, and *ii)* a homogeneous Neumann boundary condition on Γ_N, on the traction-free upper crack face, where the stress component σ_{nz} is null.

In a 2D view, we consider a semi-infinite straight crack occupying the negative part of the x-axis, with the crack tip located at the origin of the Cartesian or polar coordinate system, see Fig. 2. Since $u(\mathbf{x})$ is a harmonic function, the so-called Robin-Neumann (R-N) BVP is defined as

$$\Delta u = 0 \quad \mathbf{x} \in \Omega, \tag{23}$$

$$\sigma_{nz}(\mathbf{x}) + 2ku(\mathbf{x}) = 0 \quad \mathbf{x} \in \Gamma_R, \tag{24}$$

$$\sigma_{nz}(\mathbf{x}) = 0 \quad \mathbf{x} \in \Gamma_N. \tag{25}$$

A polar coordinate system centered at the crack tip is used to describe the analytic solution. Thus, the Robin and Neumann boundary conditions are prescribed at $\theta = 0$ and $\theta = \pi$, respectively. As shown in [26], the most singular part

of this crack tip solution is given in the form of a truncated asymptotic series

$$u(r, \theta) = K \left(1 + \sum_{k=1}^{S} u^{(k)}(r, \theta) + O(r^{S+1} \log^{S+1} r) \right), \tag{26}$$

where the parameter K is the Generalized Stress Intensity Factor (GSIF), the constant main term $u^{(0)} = 1$, and S is the number of the so-called shadow terms $u^{(k)}$ associated to the main term.

In a complete BVP, e.g., with some loads prescribed also on the outer boundary contour, the value of K depends on these loads and the geometry of the whole BVP. When S is increased, the error in the fulfillment of the Robin boundary condition decreases in a neighbourhood of the crack tip (the singular point). The number of shadow terms considered in the asymptotic series is related to computational cost and solution accuracy. The more shadow terms included, the lower the error, but at a higher computational cost.

In the present article, the behaviour of the singular solution near the crack tip is described by the asymptotic series associated with the first main term truncated at $S = 2$. Although only the first shadow term in the series is related to logarithmic singularities in stresses, an additional shadow term related to the logarithmic singularity in the gradient of boundary tractions has been included to better characterise the crack tip solution behaviour. Hence, the expressions of these two shadow terms are

$$u^{(1)}(r, \theta) = \frac{2kr}{\mu\pi} \left(\cos\theta \ln r + (\pi - \theta) \sin\theta \right),$$

$$u^{(2)}(r, \theta) = \frac{k^2 r^2}{\mu^2 \pi^2} \left(\cos 2\theta \left[\ln^2 r - \ln r - (\pi - \theta)^2 \right] + \sin 2\theta (\pi - \theta)(2\ln r - 1) \right). \tag{27}$$

The stresses corresponding to these displacements are expressed as

$$\sigma_{\theta z}(r, \theta) = -\frac{2k}{\pi} \left(\sin\theta \ln r - (\pi - \theta) \cos\theta + \sin\theta \right) + \frac{k^2 r}{\mu\pi^2} \left(\sin 2\theta \left[-2\ln^2 r + 2(\pi - \theta)^2 + 1 \right] + 4(\pi - \theta) \cos 2\theta \ln r \right), \tag{28}$$

and

$$\sigma_{rz}(r, \theta) = \frac{2k}{\pi} \left(\cos\theta \ln r + (\pi - \theta) \sin\theta + \cos\theta \right) + \frac{k^2 r}{\mu\pi^2} \left(\cos 2\theta \left[2\ln^2 r - 2(\pi - \theta)^2 - 1 \right] + 4(\pi - \theta) \sin 2\theta \ln r \right). \tag{29}$$
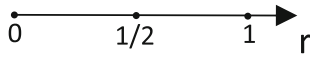
Fig. 3 One-dimensional element

These stresses have a logarithmic singularity at $r = 0$, whereas $\sigma_{\theta z}$ is bounded along the positive part of the x-axis ($\theta = 0$) near the singular point [26].

4 Singular element for logarithmic stress-singularity

Once the crack tip displacement solution given by (26) and (27) is known, a finite element capable of approximating the most relevant part of this singular solution can be developed. For ease of understanding, 1-D shape functions are derived first, and then 2-D shape functions are obtained.

4.1 1-D shape functions

In order to deduce the set of shape functions of the 1D-element represented in Fig. 3, with nodes at $r_1 = 0$, $r_2 = 0.5$ and $r_3 = 1$, the following basis functions defined in the interval [0, 1] are considered in view of (26) and (27)

$$\widetilde{N}_1(r) = 1, \quad \widetilde{N}_2(r) = r, \quad \widetilde{N}_3(r) = r \ln(r). \tag{30}$$

Then, the new 1D-element shape functions are obtained by a linear combination of the basis functions

$$N_i(r) = C_{ij}\widetilde{N}_j(r), \tag{31}$$

by imposing the well-known Lagrange interpolation property

$$N_i(r_j) = \delta_{ij}, \tag{32}$$

where δ_{ij} is the Kronecker delta. Solving the system of equations (32), the following set of functions is obtained

$$N_1(r) = 1 - r - \frac{r \ln(r)}{\ln\left(\frac{1}{2}\right)}, \tag{33}$$

$$N_2(r) = \frac{2r \ln(r)}{\ln\left(\frac{1}{2}\right)}, \tag{34}$$

$$N_3(r) = r - \frac{r \ln(r)}{\ln\left(\frac{1}{2}\right)}. \tag{35}$$

Another and equivalent method that could be used to obtain these shape functions was developed in [40]. The plots of these functions in Fig. 4 show that the maximum of $N_2(r)$ is not achieved in the associated node 2 with $r_2 = 0.5$, as usual, but in a point with $r = e^{-1} = 0.367879$. Nevertheless, it is considered that this fact has no influence on the
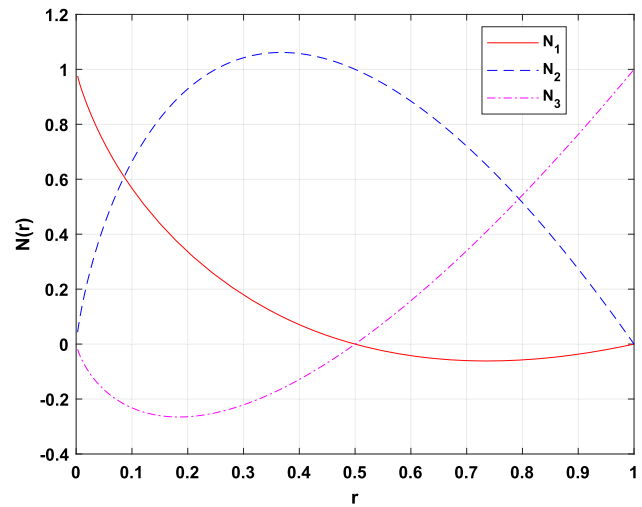

Fig. 4 One-dimensional shape functions in r

performance of the new crack-tip element defined by these functions.

It can be checked that these shape functions fulfill the rigid body translation condition

$$\sum_{i=1}^{3} N_i(r) = 1, \tag{36}$$

and the constant strain condition

$$\sum_{i=1}^{3} r_i N_i(r) = r. \tag{37}$$

It is also useful to see, especially in view of the logarithmic function included, that these functions can be transformed into a dimensionless form after being transported to a finite element of length h by the linear mapping $r \to \frac{r}{h}$, just scaling their shapes shown in Fig. 4 as

$$N_1(r) = 1 - \frac{r}{h} - \frac{r \ln(r/h)}{h \ln\left(\frac{1}{2}\right)}, \tag{38}$$

$$N_2(r) = \frac{2r \ln(r/h)}{h \ln\left(\frac{1}{2}\right)}, \tag{39}$$

$$N_3(r) = \frac{r}{h} - \frac{r \ln(r/h)}{h \ln\left(\frac{1}{2}\right)}. \tag{40}$$

4.2 2-D shape functions

Once the shape functions have been obtained in 1-D space, it is necessary to generalise them to a 2-D reference space ξ - η, with $0 \le \xi, \eta \le 1$. This is done by generating a square reference element with 6 nodes and shape functions with linear behaviour in η and with variation of 1-D special shape functions in ξ, by replacing r with ξ in (33)–(35).

Table 1 Displacement shape functions

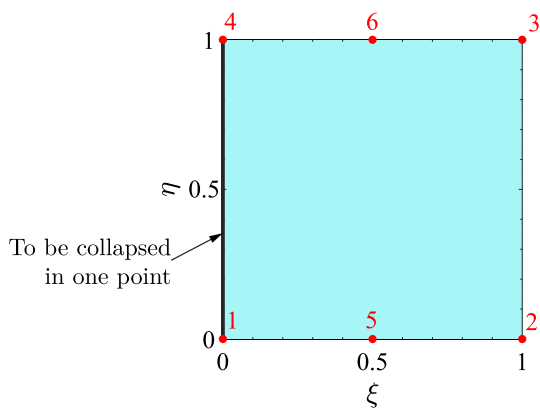| i	N_i^u	$\frac{\partial N_i^u}{\partial \xi}$	$\frac{\partial N_i^u}{\partial \eta}$
1	$(1-\eta)\left(1 - \xi - \xi\frac{\ln(\xi)}{\ln(1/2)}\right)$	$(1-\eta)\left(-1 - \frac{1}{\ln(1/2)} - \frac{\ln(\xi)}{\ln(1/2)}\right)$	$-\left(1 - \xi - \xi\frac{\ln(\xi)}{\ln(1/2)}\right)$
2	$(1-\eta)\left(\xi - \xi\frac{\ln(\xi)}{\ln(1/2)}\right)$	$(1-\eta)\left(1 - \frac{\ln(\xi)}{\ln(1/2)} - \frac{1}{\ln(1/2)}\right)$	$-\left(\xi - \xi\frac{\ln(\xi)}{\ln(1/2)}\right)$
3	$\eta\left(\xi - \xi\frac{\ln(\xi)}{\ln(1/2)}\right)$	$\eta\left(1 - \frac{\ln(\xi)}{\ln(1/2)} - \frac{1}{\ln(1/2)}\right)$	$\left(\xi - \xi\frac{\ln(\xi)}{\ln(1/2)}\right)$
4	$\eta\left(1 - \xi - \xi\frac{\ln(\xi)}{\ln(1/2)}\right)$	$\eta\left(-1 - \frac{1}{\ln(1/2)} - \frac{\ln(\xi)}{\ln(1/2)}\right)$	$\left(1 - \xi - \xi\frac{\ln(\xi)}{\ln(1/2)}\right)$
5	$(1-\eta)\left(2\xi\frac{\ln(\xi)}{\ln(1/2)}\right)$	$2(1-\eta)\left(\frac{\ln(\xi)}{\ln(1/2)} + \frac{1}{\ln(1/2)}\right)$	$-\left(2\xi\frac{\ln(\xi)}{\ln(1/2)}\right)$
6	$\eta\left(2\xi\frac{\ln(\xi)}{\ln(1/2)}\right)$	$2\eta\left(\frac{\ln(\xi)}{\ln(1/2)} + \frac{1}{\ln(1/2)}\right)$	$\left(2\xi\frac{\ln(\xi)}{\ln(1/2)}\right)$

Fig. 5 Quadrilateral element in the reference space

Fig. 6 Collapsed triangular element in the physical space

Table 2 Geometric shape functions

i	N_i^g	$\frac{\partial N_i^g}{\partial \xi}$	$\frac{\partial N_i^g}{\partial \eta}$
1	$(1-\xi)(1-\eta)$	$-(1-\eta)$	$-(1-\xi)$
2	$\xi(1-\eta)$	$(1-\eta)$	$-\xi$
3	$\xi\eta$	η	ξ
4	$(1-\xi)\eta$	$-\eta$	$(1-\xi)$

The set of the obtained 2-D shape functions and their derivatives are shown in Table 1 with the numbering associated to nodes defined in Fig. 5. These shape functions are used to approximate displacements and their derivatives, strains and stresses, and are fundamental for computing the stiffness matrix.

However, for modelling the geometry and the Jacobian matrix, standard bilinear shape functions are used, see Table 2.

4.2.1 Singular shape functions in the collapsed triangular element

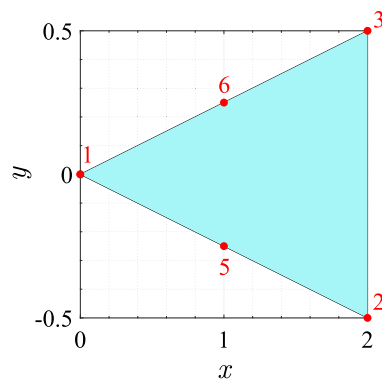The mapping between the quadrilateral element, in the reference $\xi - \eta$ space, and the triangular element, in the physical $x - y$ space, is defined by the bilinear geometric shape functions together with the collapse of the element side between nodes 1 and 4 (Fig. 5) into a point, following [33]. Notice that the logarithmic shape functions in the quadrilateral element have an infinite gradient at this element side. Thus, the logarithmic stress-singularity along the side 1–4 is collapsed into a logarithmic stress-singularity in node 1. Hence, the variation of the resulting displacement shape functions defined in the triangular element in the $x - y$ space is considered appropriate for approximation of the logarithmic stress-singularity.

In Fig. 6, the collapse of all the points on the rectangular element side 1–4 ($\xi = 0$) into one point defined by node 1 in the new triangular element is illustrated.

The plots of the developed displacement shape functions in the rectangular and triangular elements, respectively, in the $\xi - \eta$ and $x - y$ spaces, are depicted in Figs. 7 and 8. It is important to notice that in these plots there is a logarithmic variation in the ξ-direction while maintaining a linear variation in the η-direction.

As explained above, all the points on the $\xi = 0$ side collapse into a single point defined by the node 1 generating a new singular function in the $x - y$ space given by the summation of two displacement functions in the $\xi - \eta$ space

$$[N_1(\xi, \eta) + N_4(\xi, \eta)]_{\xi-\eta \text{ space}} = [N_1(x, y)]_{x-y \text{ space}} \quad (41)$$
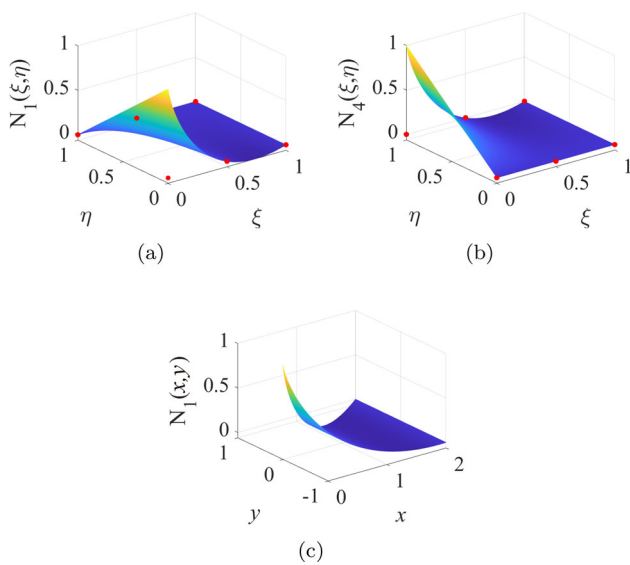
Fig. 7 Shape functions of the rectangular element represented in the reference space **a** N_1 and **b** N_4. **c** N_1 shape function of the collapsed triangular element in the physical space

Note that depending on the domain discretization in the physical $x - y$ space, special triangular elements with the logarithmic stress-singularity can have different triangular forms.

4.3 Stiffness matrix

Starting from the above weak formulation of the considered BVP, the part of the bilinear form on the left-hand side of (10) associated with the element Ω_n with the trial displacements u and test displacements v is given by

$$\mu \int_{\Omega_n} \left(\frac{\partial v}{\partial x} \ \frac{\partial v}{\partial y} \right) \begin{pmatrix} \frac{\partial u}{\partial x} \\ \frac{\partial u}{\partial y} \end{pmatrix} dx dy + 2k \int_{\Gamma_{Rn}} uv \, d\ell, \tag{42}$$

$d\ell$ being the differential element of length on Γ_{Rn}. Note that Γ_{Rn} can be empty for some elements. Then, the change of variable can be defined using the Jacobian matrix

$$\begin{pmatrix} \frac{\partial u}{\partial \xi} \\ \frac{\partial u}{\partial \eta} \end{pmatrix} = [J] \begin{pmatrix} \frac{\partial u}{\partial x} \\ \frac{\partial u}{\partial y} \end{pmatrix}, \tag{43}$$

leading to the final expression for the bilinear form for the element Ω_n

$$\mu \int_0^1 \int_0^1 \left(\frac{\partial v}{\partial \xi} \ \frac{\partial v}{\partial \eta} \right) ([J]^{-1})^T [J]^{-1} \begin{pmatrix} \frac{\partial u}{\partial \xi} \\ \frac{\partial u}{\partial \eta} \end{pmatrix} |J| d\xi d\eta$$

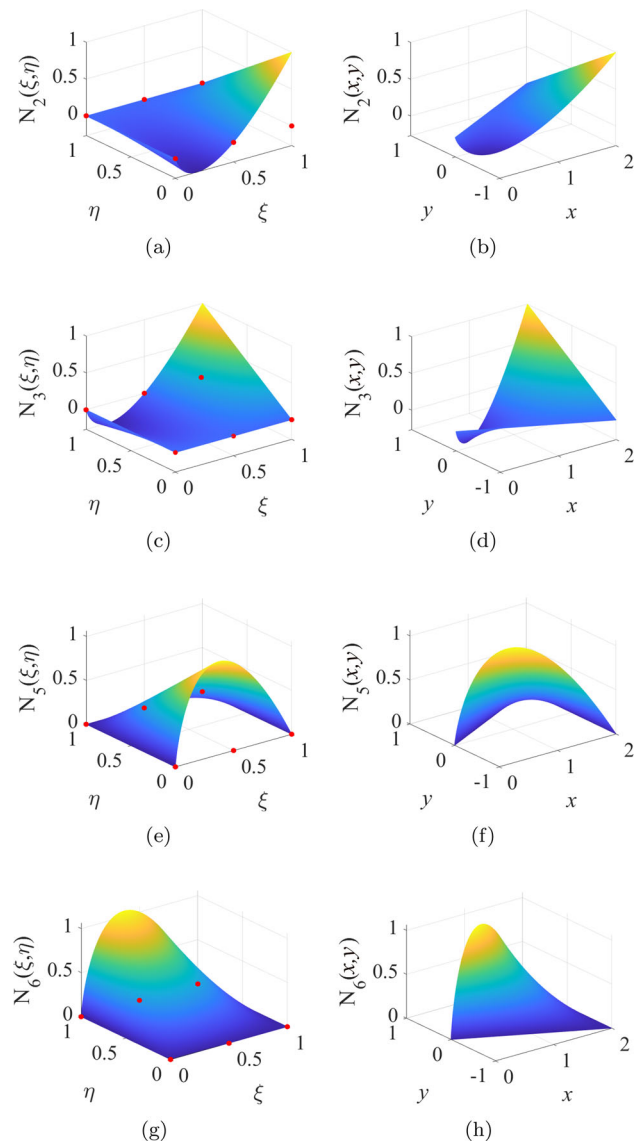$$+ \chi_{Rn} 2k \int_0^1 uv \frac{d\ell}{d\xi} d\xi, \tag{44}$$

Fig. 8 Shape functions of the rectangular element represented in the reference space. **a** N_2, **c** N_3, **e** N_5, **g** N_6. Shape functions of the collapsed triangular element in the physical space **b** N_2, **d** N_3, **f** N_5, **h** N_6

where χ_{Rn} is equal to 1 when the element Ω_n has a Robin condition on one of its edges, otherwise it is zero. For a singular element, this element edge is associated with a constant value of η, which is either 0 or 1 depending on the location of the Robin boundary, see Fig. 5. The displacement fields u and v can be approximated using the same displacement shape functions

$$u = \sum_{i=1}^{6} N_i(\xi, \eta) u_i, \tag{45}$$

$$v = \sum_{i=1}^{6} N_i(\xi, \eta) v_i. \tag{46}$$

Then, their derivatives in the reference space are

$$\frac{\partial u}{\partial \xi} = \sum_{i=1}^{6} \left(\frac{\partial N_i(\xi, \eta)}{\partial \xi} u_i \right), \tag{47}$$

$$\frac{\partial v}{\partial \xi} = \sum_{i=1}^{6} \left(\frac{\partial N_i(\xi, \eta)}{\partial \xi} v_i \right), \tag{48}$$

$$\frac{\partial u}{\partial \eta} = \sum_{i=1}^{6} \left(\frac{\partial N_i(\xi, \eta)}{\partial \eta} u_i \right), \tag{49}$$

$$\frac{\partial v}{\partial \eta} = \sum_{i=1}^{6} \left(\frac{\partial N_i(\xi, \eta)}{\partial \eta} v_i \right). \tag{50}$$

The $[B]$ matrix and $[N]$ vector can be defined, taking into account the collapse of the edge between nodes 1 and 4 to get the triangular element in the physical space as

$$[B] = \begin{pmatrix} \frac{\partial(N_1+N_4)}{\partial \xi} & \frac{\partial(N_1+N_4)}{\partial \eta} \\ \frac{\partial N_2}{\partial \xi} & \frac{\partial N_2}{\partial \eta} \\ \vdots & \vdots \\ \frac{\partial N_6}{\partial \xi} & \frac{\partial N_6}{\partial \eta} \end{pmatrix}, \quad [N] = \begin{pmatrix} (N_1+N_4) \\ N_2 \\ \vdots \\ N_6 \end{pmatrix}. \tag{51}$$

Then, the 5×5 element stiffness matrix is generated in the form

$$(K_{ij})_{5x5} = \mu \int_0^1 \int_0^1 [B]([J]^{-1})^T [J]^{-1} [B]^T |J| d\xi d\eta$$
$$+ \chi_{Rn} 2k \int_0^1 [N][N]^T \frac{d\ell}{d\xi} d\xi. \tag{52}$$

The elements of this matrix can be computed either numerically or analytically. In the present article, the calculations are carried out by analytical integrations using the computer algebra software Mathematica [41], to avoid any numerical issues. However, some preliminary results have also been obtained by using the Gauss quadrature method combined with an appropriate coordinate transformation. The results obtained by both approaches have almost the same accuracy with at least 10 identical significant digits.

5 Numerical results and convergence study

First, to check the implementation of the new special singular element and to ensure the convergence of the FEM solutions using this element, it was successfully tested by solving various patch tests with spring boundary conditions.

5.1 Definition of the analysed meshes and problems

An h-refinement of uniform meshes is employed to analyse the convergence behaviour of the new crack-tip triangular element for cracks propagating along spring interfaces. Standard linear triangular elements are used in the whole domain except for the neighbourhood of the crack tip, where the crack-tip elements are used. For comparison purposes, the same meshes using the standard linear triangular elements in the whole domain, including the crack tip neighbourhood, are also employed. For these studies, a unit square domain discretised by triangular elements is considered.

The results are obtained by the above described FEM implementation in the software Matlab [42]. Three different types (patterns) of meshes are used as well as different number of elements that compose them. The mesh patterns are shown in Fig. 9. The mesh of type 3 is based on the suggestions for classical quarter-point elements for a better performance [33, 34]. Specifically, when quarter-point elements are used, isosceles triangles are recommended with the unequal angle located at the crack tip. Following this idea, the mesh of type 3 has the same number of elements at the crack tip as the mesh of type 2 but using isosceles triangles at the crack tip. The mesh of type 3 is obtained from the mesh of type 2 by radially moving one vertex of the triangular crack tip elements to achieve that all triangles at the crack tip are isosceles. Thus, only the crack tip elements and the surrounding ones are modified. Nevertheless, further analyses will be necessary to propose some general rules regarding the optimal convergence properties of the proposed element, especially when a different type of regular local mesh is used, that may include elements within one or two circular-ring zones surrounding the crack tip elements.

The total number of elements in a mesh is defined by a parameter N, where $2N$ is the number of elements along each square side. The spring (Robin) and traction free (homogeneous Neumann) boundary conditions are prescribed on the right and left halves of the bottom edge, respectively. Thus, N can be also defined as

$$N = \frac{a}{h}, \tag{53}$$

where a is the length of the traction free zone, usually associated to the crack (half-)length, and h is the characteristic length of an element.

Figure 10 shows the two benchmark problems analysed with the above described meshes. The length of the square domain side is $L = 2a = 1$ in all cases as mentioned above.

The first analysed problem, in Fig. 10a, is based on the most singular term of the asymptotic series at tip of a semi-infinite crack in Mode III located on a flat spring interface (26), a solution studied in [25–27]. This solution is, to the best of the authors' knowledge, the only analytical solution

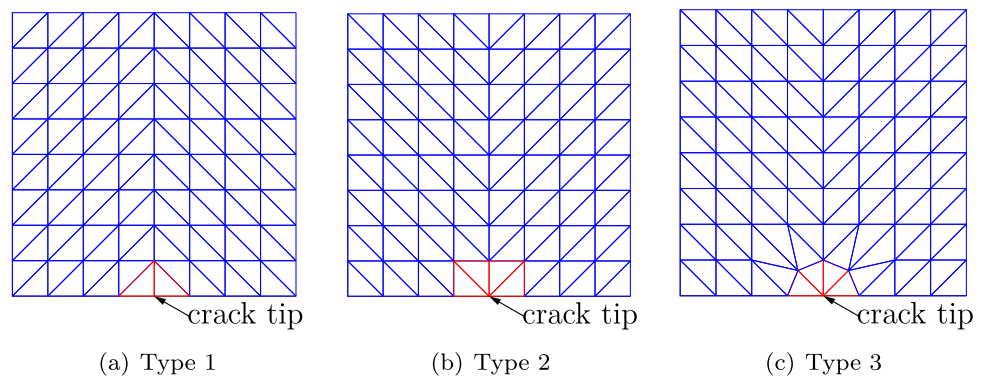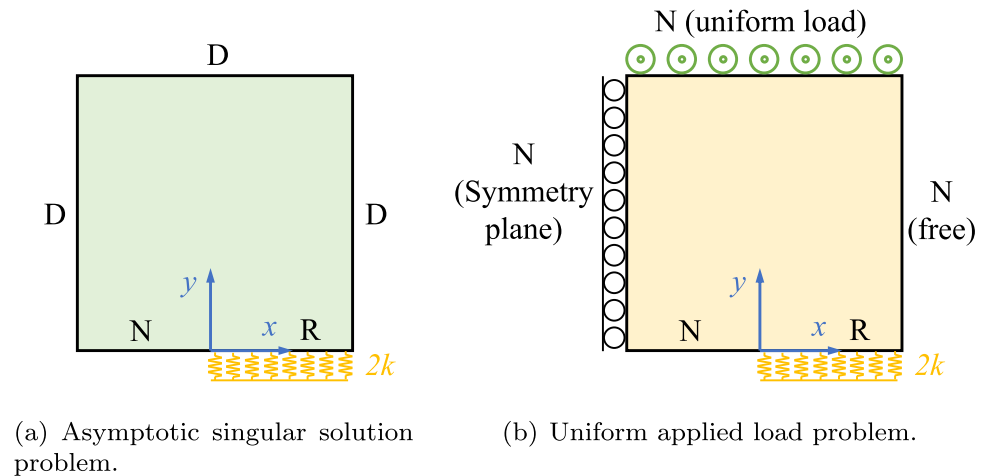**Fig. 9** Analysed mesh patterns for N=4

(a) Type 1   (b) Type 2   (c) Type 3

Fig. 10 Boundary conditions of the two analysed problems. D, N and R are associated to Dirichlet, Neumann and Robin boundaries, respectively

(a) Asymptotic singular solution problem.

(b) Uniform applied load problem.

currently available for a crack in a spring interface. The displacement on the edges with Dirichlet boundary conditions is imposed by this singular term. The problem parameters are: shear modulus $\mu = 1$, spring stiffness $2k = 1$, GSIF $K = 1$, and the number of shadow terms used in the truncated series is $S = 10$ in (26).

The second problem is shown in Fig. 10b, where the uniform Neumann boundary conditions with $\tau = \sigma_{yz} = 1$ is applied on the upper edge, the Robin boundary condition on the right half part of the lower edge and the remaining edges are stress free boundaries. It will be referred to as the uniform applied load problem. Due to the nature of the antiplane problem, particularly regarding the meaning of the stress free boundary, this problem could represent three different problems: (a) actual stress free boundaries on the left and right edges, (b) left edge representing a symmetry plane, thus the model describes half of the solid, and (c) both left and right edges representing symmetry planes, thus the model also represents the configuration of an infinite array of periodic cracks along the x-axis, cf. Appendix A.

5.2 Asymptotic singular solution problem

The numerical solutions obtained using only the standard elements, and by using also the new singular elements with

the logarithmic stress-singularity at the crack tip, are compared with the analytical expression of the asymptotic crack tip solution (26) developed in [26]. For the calculation of the analytical solution $S = 10$ shadow terms have been used. The relative error of the numerical solution for displacement obtained with respect to the analytical solution is evaluated to study which numerical solutions approximate better the analytical solution.

Figure 11 shows the numerical solutions in displacement for the mesh type 2. The solutions obtained by using the standard elements, the singular elements, as well as the analytical solution [26] are compared. A rapid convergence of all numerical solutions to the analytical solution is observed. This is a relevant confirmation of the correct FEM implementation for the Robin BVP according to Sect. 2, in fact this is one of the reasons to first compare the numerical results with the only analytical solution currently available. The singular elements give more accurate solutions than standard elements as expected. However, the improvement is not so great because the stiffness of the spring distribution is relatively low, as according to Sect. 5.3 the improvement increases with the spring stiffness, which makes the Robin BVP with the logarithmic stress-singularity at the crack tip more difficult to solve numerically.
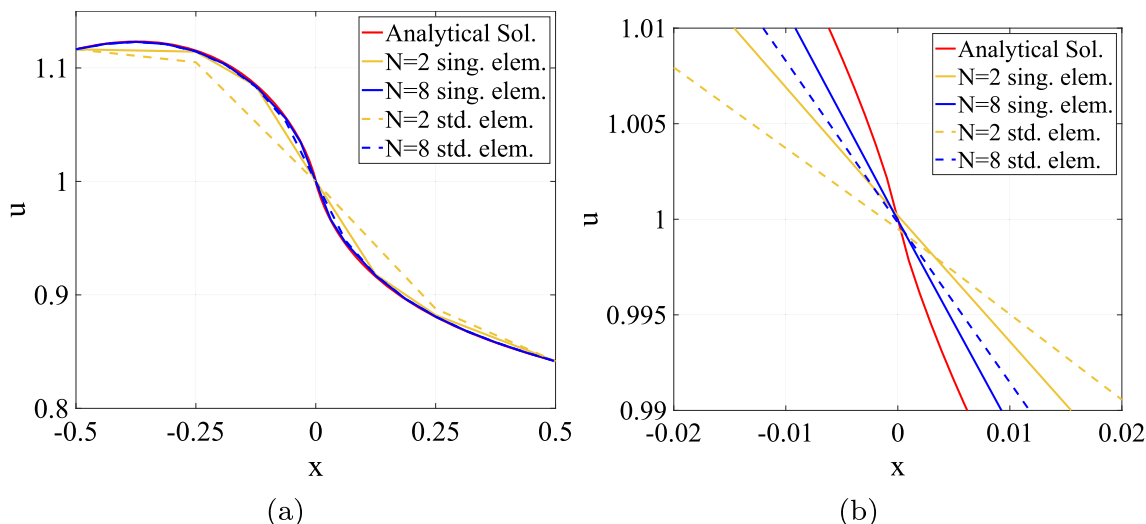
Fig. 11 Numerical solutions for displacement obtained for the mesh type 2 along the bottom edge in the asymptotic singular solution problem **a** global view and **b** zoom
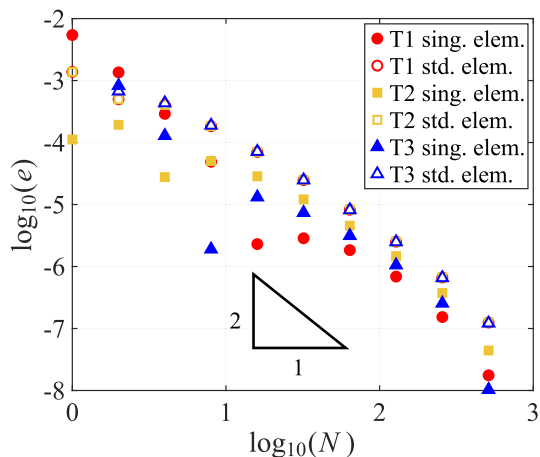

Fig. 12 Convergence of the relative error e in the crack tip displacement obtained for each numerical solution of the asymptotic singular solution problem. T1, T2 and T3 correspond to the mesh type 1, 2 and 3, respectively

In Fig. 12, the convergence of the relative error in displacement at the crack tip, $e = |u_{num} - u_{ana}|/u_{ana}$, for increasing values of N, obtained for each numerical solution and the mesh type with respect to the analytical solution is shown in a log-log plot. A triangle in the plot indicates the expected quadratic asymptotic convergence rate $O(N^{-2})$ for these elements. A non-monotonous convergence of e is observed in

some cases for coarse meshes. It is associated to a change of sign of the absolute error $u_{num} - u_{ana}$. This behaviour is observed for all numerical solution obtained by singular elements.

It can be observed that as the value of N increases the numerical solutions converge to the analytical one, with relative errors up to 10^{-8} being achieved. This provides an additional confirmation of the correct FEM implementation for the Robin BVP according to Sect. 2. In general, with some exceptions for the coarsest meshes, the singular elements give consistently smaller errors, often by an order of magnitude, than the standard elements. The error of the standard elements is essentially insensitive to the mesh pattern, whereas the singular elements may give different errors for different mesh patterns.

To check the improvement by the developed singular elements, the ratio of the relative error with respect to the analytical solution for the crack tip displacement is evaluated using the improvement ratio

$$I = \frac{e_{std}}{e_{sing}}, \tag{54}$$

where e_{std} and e_{sing} are the relative errors obtained using the standard elements and the new singular elements, respectively, for the same mesh type. Table 3 summarizes the results

Table 3 Improvement obtained when the new singular element is used in the asymptotic singular solution problem

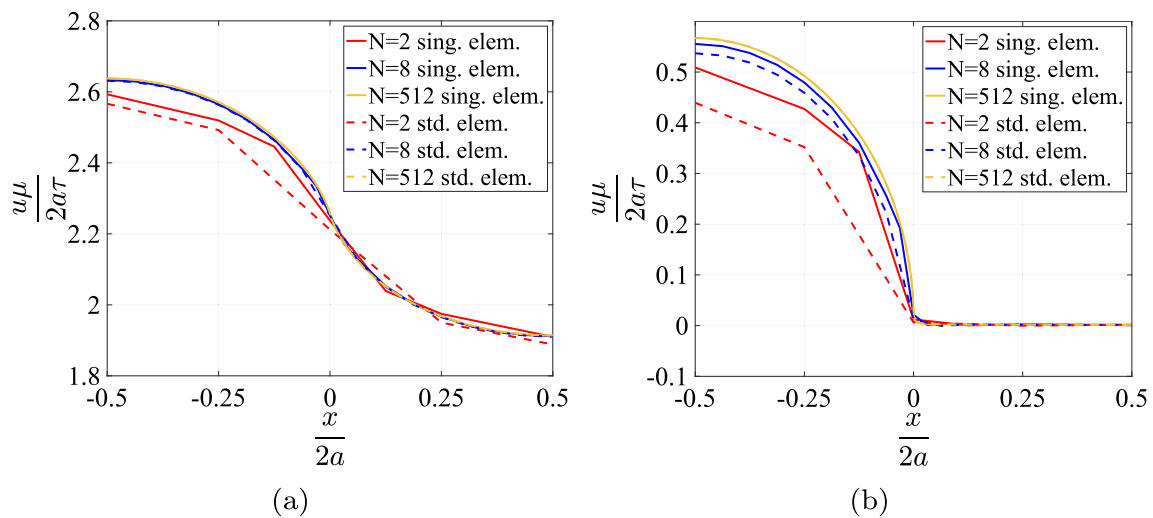| Pattern \ N	1	2	4	8	16	32	64	128	256	512
1	0.3	0.4	1.4	3.8	30.8	8.7	4.5	3.7	4.4	7.1
2	12.3	2.6	14.6	3.6	2.5	2.0	1.8	1.7	1.8	2.8
3	–	0.8	3.4	99.5	5.4	3.4	2.6	2.4	2.6	11.8

Fig. 13 Numerical solutions obtained for the mesh type 1 for **a** $\delta = 1$ and **b** $\delta = 1000$, in the uniform applied load problem
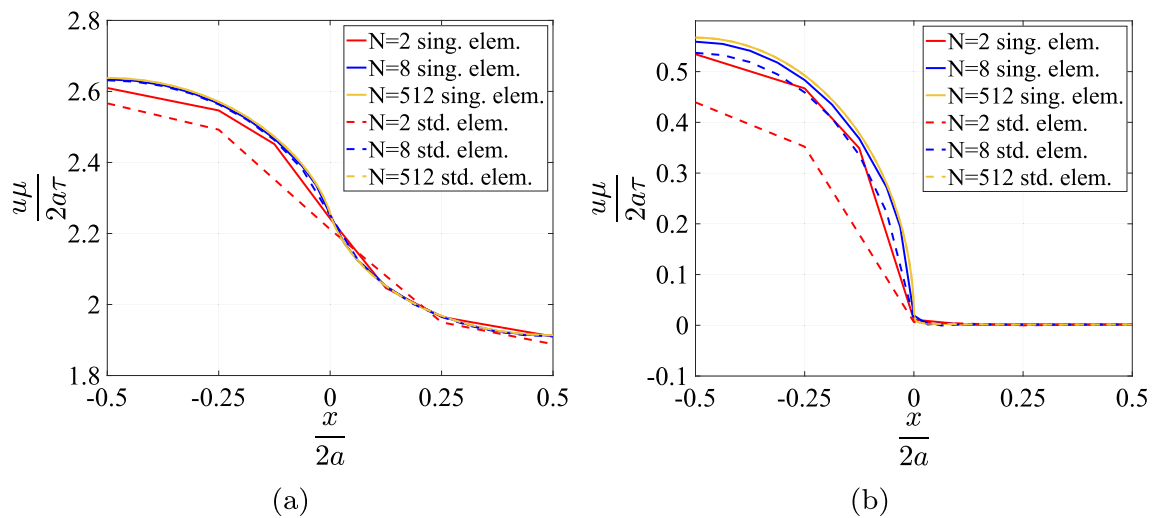

Fig. 14 Solutions obtained for the mesh type 2 for **a** $\delta = 1$ and **b** $\delta = 1000$, in the uniform applied load problem

for the obtained improvements when the new singular elements are used, for every mesh pattern and several N values. The results obtained using singular elements always give more accurate results for mesh type 2, while the same occurs for the mesh types 1 and 3 for $N \geq 4$.

5.3 Uniform applied load problem

For this problem, several spring stiffness values are tested by varying the value of the dimensionless structural parameter δ, while keeping the model geometry fixed, cf. [5],

$$\delta = \frac{2kL_{\text{ch}}}{\mu} = \frac{4ka}{\mu}, \tag{55}$$

where k is the spring stiffness (in the complete problem), L_{ch} is a characteristic length of the problem (the crack length $2a$

is used herein) and μ is the material shear modulus. The considered δ values are 0.1, 1, 10, 100 and 1000.

Figures 13, 14 and 15 show the displacement field along the bottom edge obtained for the three types of analysed meshes and for two values of δ. It seems that the numerical solutions tend to the perfect interface solution when the stiffness of the interface is sufficiently large. As expected, the solutions obtained using the singular elements are more accurate and converge faster to the solution obtained using the finest mesh than those obtained using the standard elements. These differences are more evident for the very stiff spring distribution with $\delta = 1000$.

Analogously to the previous section, the improvement achieved in the crack-tip solution when using the singular elements is analysed. In the asymptotic singular solution problem, the numerical solutions converged to the analytical
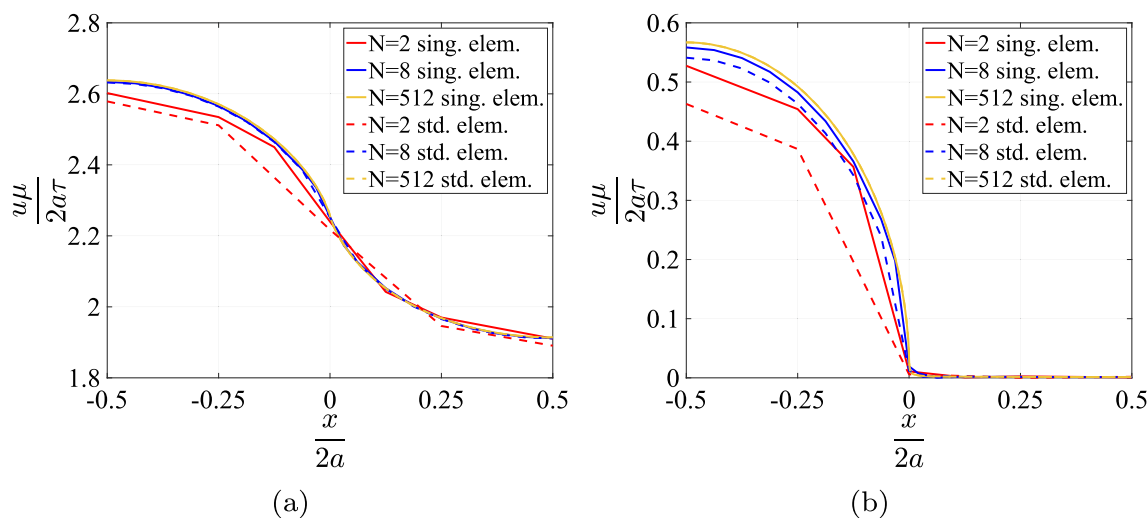
Fig. 15 Solutions obtained for the mesh type 3 for **a** $\delta = 1$ and **b** $\delta = 1000$, in the uniform applied load problem

solution as the value of N increased. In the current problem, no analytical solution is available. Thus, a way to calculate the error is by taking as a reference the results obtained with the finest mesh (i.e. the largest number of elements in the Robin boundary part) in this case $N = 512$, for each mesh pattern and the kind of finite elements used. The relative error for this problem can be defined equivalently in terms of either the crack-tip displacement or the crack-tip shear calculated on the Robin boundary part as

$$e_{\text{rel}} = \frac{u_{\text{tip}}(N) - u_{\text{tip}}(N_{\max})}{u_{\text{tip}}(N_{\max})} = \frac{\tau_{\text{tip}}(N) - \tau_{\text{tip}}(N_{\max})}{\tau_{\text{tip}}(N_{\max})}. \quad (56)$$

Figure 16 shows the variation of this relative error as the number of elements N in the Robin boundary part increases, for $\delta = 0.1, 1, 10, 100$ and 1000. The results show that when the interface stiffness is small i.e. $\delta = 0.1$ and 1, the relative errors are very similar for all considered types of meshes and types of finite elements. The main differences occur for the smallest values of N. On the other hand, when the interface stiffness becomes higher, i.e. $\delta \geq 10$, the differences between the meshes with and without singular elements become evident, especially for the large values of N, where the errors obtained using singular elements are significantly smaller than those obtained using standard elements only, often by an order of magnitude or more.

In Fig. 17, the dimensionless shear stress values at the crack tip (defined from the Robin boundary side) are plotted with respect to N. The results for the meshes with and without singular elements are depicted for $\delta = 0.1, 1, 10, 100$ and 1000. These results show that the solutions for each kind of mesh tend to a constant value (converged solution) for sufficiently large values of N. The asymptote lines shown in the plots represent the values obtained for the highest N value for each mesh pattern and using singular elements. When the

interface stiffness is small ($\delta \leq 1$), the shear stress value at the crack tip is well approximated even for small values of N (coarse meshes). However, as the interface becomes stiffer ($\delta \geq 10$), the convergence of the numerical solution is slower because larger values of N are needed to obtain a constant value. The crack-tip shear stress values for all kinds of meshes tend to approximately the same value for the highest value of N, for $\delta \leq 100$, whereas for $\delta = 1000$ they tend to only slightly different values. Noteworthy, the numerical solutions converge significantly faster when the singular elements are used.

The convergence of the Energy Release Rate (ERR) G_{tip} (in its dimensionless form) at the crack tip is presented in Fig. 18. Recall that G_{tip} is usually the most relevant quantity for prediction of crack propagation along spring interfaces. In [26] it was shown that G_{tip} values in a spring-like interface, associated to fracture Mode III, can be calculated by the following expressions

$$G_{\text{tip}} = \tau_{\text{tip}} u_{\text{tip}} = \frac{\tau_{\text{tip}}^2}{2k} = 2k u_{\text{tip}}^2. \quad (57)$$

Thus, G_{tip} can be directly computed using the crack tip displacement u_{tip}. The values of G_{tip} computed using meshes with and without singular elements varying the number of elements N are plotted in Fig. 18 for $\delta = 0.1, 1, 10, 100$ and 1000. Similarly to the results for the crack-tip shear stress, G_{tip} tends to a constant value (converged solution) for sufficiently high values of N. When the interface stiffness is small, i.e. $\delta \leq 1$, an excellent approximation of G_{tip} value is obtained even for small values of N (coarse meshes). However, when the interface becomes stiffer, i.e. $\delta \geq 10$, the convergence of G_{tip} is slower (larger N values are needed) to get an asymptotic value. Noteworthy, the values of G_{tip} for
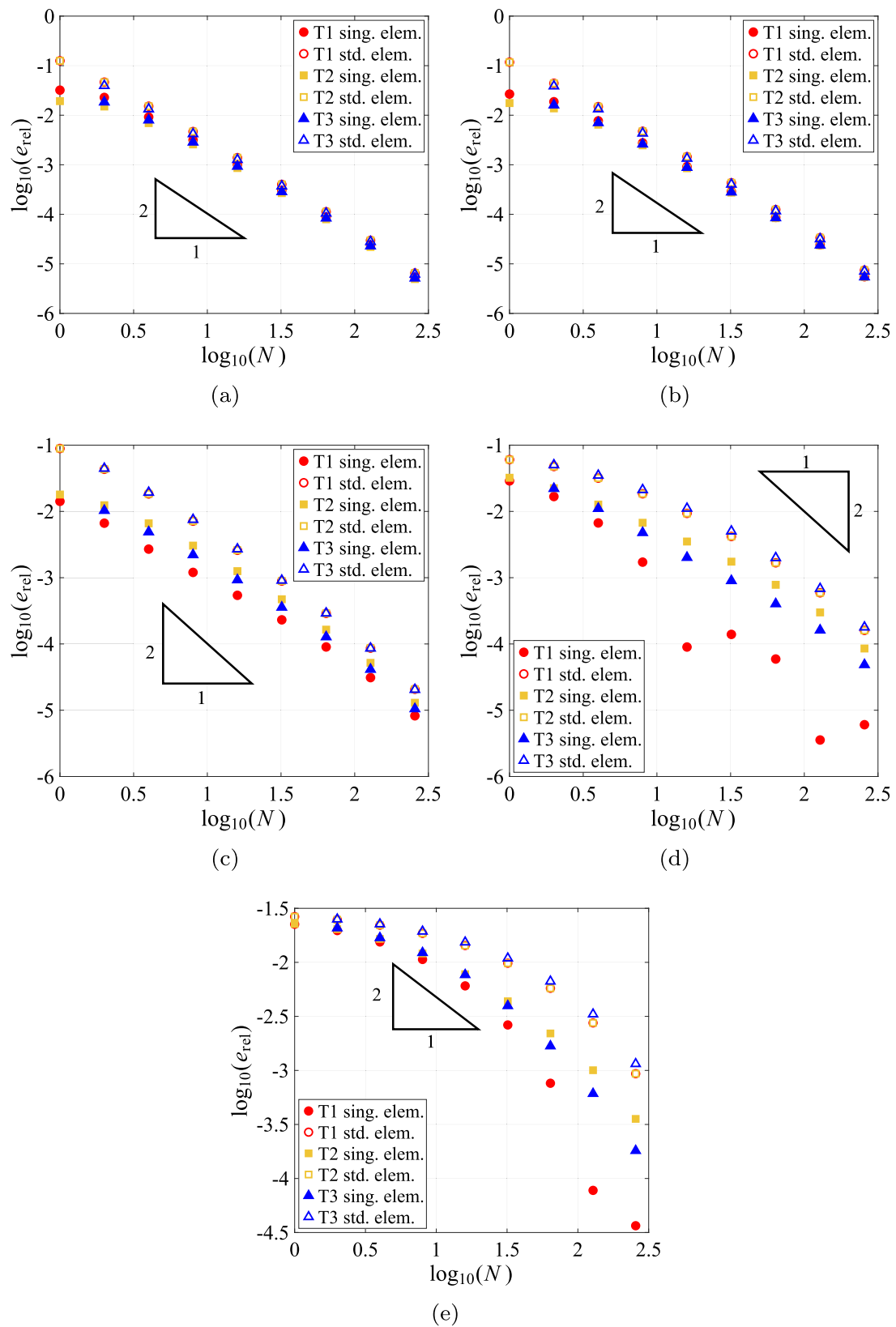
Fig. 16 The convergence of the error e_{rel} with respect to the number of elements on the Robin boundary part N for **a** $\delta = 0.1$, **b** $\delta = 1$, **c** $\delta = 10$, **d** $\delta = 100$ and **e** $\delta = 1000$, in the uniform applied load problem. T1, T2 and T3 correspond to the mesh type 1, 2 and 3, respectively
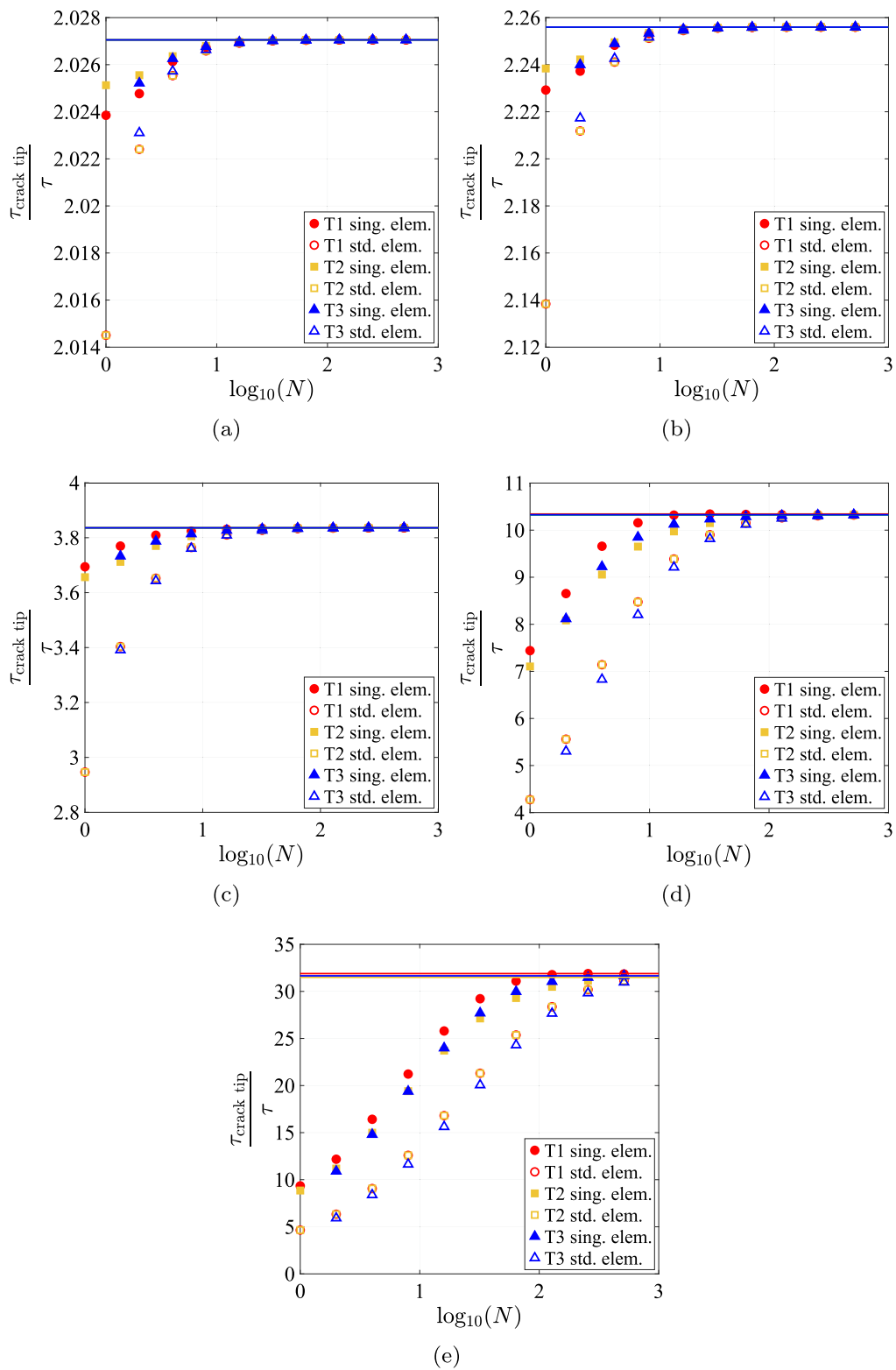
Fig. 17 The convergence of the shear stress at the crack tip with respect to the number of elements on the Robin boundary part N for **a** $\delta = 0.1$, **b** $\delta = 1$, **c** $\delta = 10$, **d** $\delta = 100$ and **e** $\delta = 1000$, in the uniform applied load problem. T1, T2 and T3 correspond to the mesh type 1, 2 and 3, respectively

all kinds of meshes tend to approximately the same asymptotic value for the highest value of N, for $\delta \leq 100$, but they tend to slightly different values for $\delta = 1000$. Again, the G_{tip} values converge significantly faster when the singular elements are used.

The G_{tip} values in Fig. 18 are normalised by the value $G_{\text{tip}} = 2a\tau^2/\mu$ obtained in an analogous problem for $k \to \infty$ (perfect interface or equivalently a crack in a homogeneous body) and infinitely long strip of width $2L = 4a$, see (A.4). As might be expected, for the higher values of δ the normalised value of G_{tip} tends to one, showing that the solutions for very stiff spring interfaces tend to the crack solution in a homogeneous body.

A comprehensive mathematical analysis of the asymptotic behaviour of the displacement solution in neighbourhood of the crack tip, for $\delta \to \infty$, was developed by Costabel and Dauge [20], focusing on the limit change from the Robin-Neumann problem (studied in the present work) to the Dirichlet-Neumann problem (corresponding to the classical crack in a homogeneous body). Costabel and Dauge [20] were able to precisely describe the change of the nature of the local solution behaviour at the crack tip from the logarithmic singularity to the classical square root singularity of stresses. According to [20, 43] and for relatively large δ values, if δ value is increased by a factor the radius of the (inner) region at the crack tip where the first most singular term of the order $r \ln r$, see (26) and (27), governs the displacement solution decreases by the same factor, and then the (outer) region governed by the classical square root solution $\sqrt{r}$ extends towards the crack tip. Thus, in the limit case only the classical square root solution governs the displacement solution near the crack tip. Such convergence, for increasing values of δ, of the numerical displacement solutions to the classical analytic solution for a crack in the homogeneous body, deduced in Appendix A, is shown in Fig. 19.

Table 4 summarizes the obtained improvement ratios I, computed analogously as in (54) but using (56), for all mesh patterns and N values. Noteworthy, the results obtained using singular elements always produced more accurate results, i.e. $I > 1$, for all mesh types and interface stiffness defined by δ values. It should be noted that, especially for large δ values, the improvement ratios I would be significantly higher if the more accurate results obtained by the singular elements were also used as reference values in the calculation of the relative error for the standard elements.

In the present model, the different values of δ were obtained by keeping the domain fixed and changing the spring stiffness. However, it was found that similar results can be obtained by changing the dimensions of the domain and keeping the stiffness of interface constant.

Conclusions and future developments

A new singular finite element for the logarithmic stress-singularities has been developed. It is capable of significantly improving the accuracy of FEM solutions for cracks growing along the Winkler-type spring interfaces between linear elastic adherents. The proposed shape functions are based on the asymptotic elastic solution with logarithmic stress-singularity at the interface crack tip, considering spring-like interface behaviour under fracture Mode III, recently deduced in [26]. They reproduce the radial behaviour of the asymptotic solution. The special crack-tip finite element developed is triangular with 5 nodes, obtained by collapsing a 6-node rectangular element.

The new finite element is implemented in a FEM code written in Matlab. The obtained numerical results show that the new element allows to model interface cracks without the need of using excessively refined FEM meshes, even for stiff interfaces. A convergence analysis using h-refinement with uniform meshes show that the new singular element provides significantly more accurate results than the standard finite elements, especially for stiff interfaces. The use of the proposed element will allow to minimize computational resources when modelling cracks propagating along stiff and thin adhesively bonded interfaces using the Linear-Elastic Brittle Interface Model (LEBIM) or the Coupled Criterion of Finite Fracture Mechanics (CC-FFM) applied to spring interfaces.

This new finite element can be applied to any other physical problems governed by the Laplace equation with the logarithmic singularities of the solution gradient at some points.

Noteworthy, new analytical expressions for the double asymptotic series at the tip of a crack located in a Winkler-type interface under fracture Mode I/II were recently deduced in [44]. These expressions show that the singular character of the crack-tip solutions in mode I/II, governed by the Lamé system, is similar to that of cracks in Mode III, governed by the Laplace equation, although with some particularities. Thus, it is expected that the FEM solution for such cracks under fracture Mode I/II can be improved using a similar crack-tip element with the logarithmic stress-singularity as the one proposed in the present article.

Nevertheless, from the present analysis of the convergence behaviour of the numerical solutions obtained by the developed singular element, and also from the discussion of the main results of the asymptotic analysis in [20, 43], see Sect. 5.3, we might expect that another singular element with a higher number of shape functions and nodes, including in addition to the 1D basis functions in (30) an additional basis function $\widetilde{N}_4(r) = \sqrt{r}$, could provide even better convergence properties covering well also cases with very large values of δ, when a large part of the crack tip element is governed by
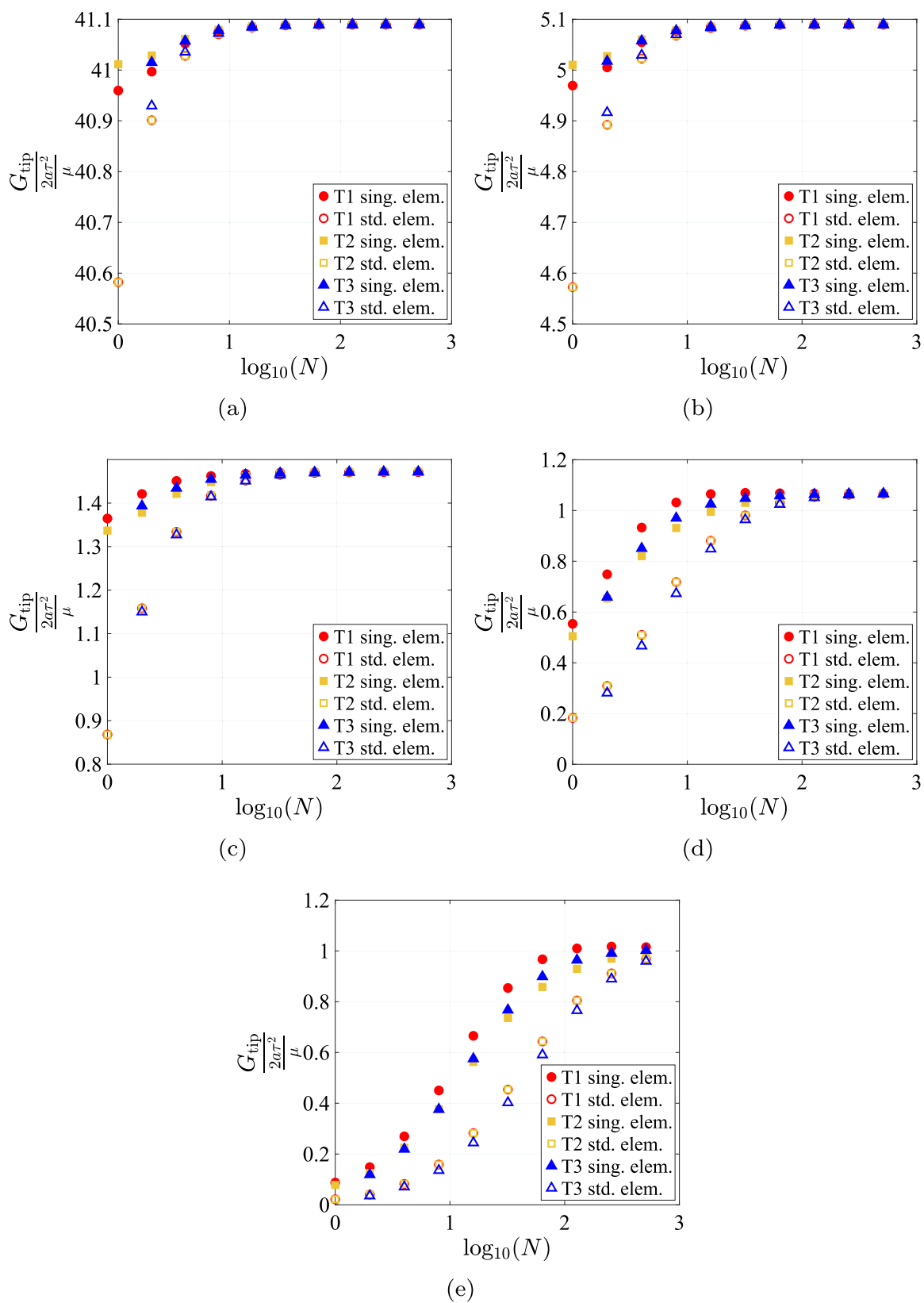
Fig. 18 The convergence of the ERR G_{tip} with respect to the number of elements on the Robin boundary part N for **a** $\delta = 0.1$, **b** $\delta = 1$, **c** $\delta = 10$, **d** $\delta = 100$ and **e** $\delta = 1000$, in the uniform applied load problem. T1, T2 and T3 correspond to the mesh type 1, 2 and 3, respectively
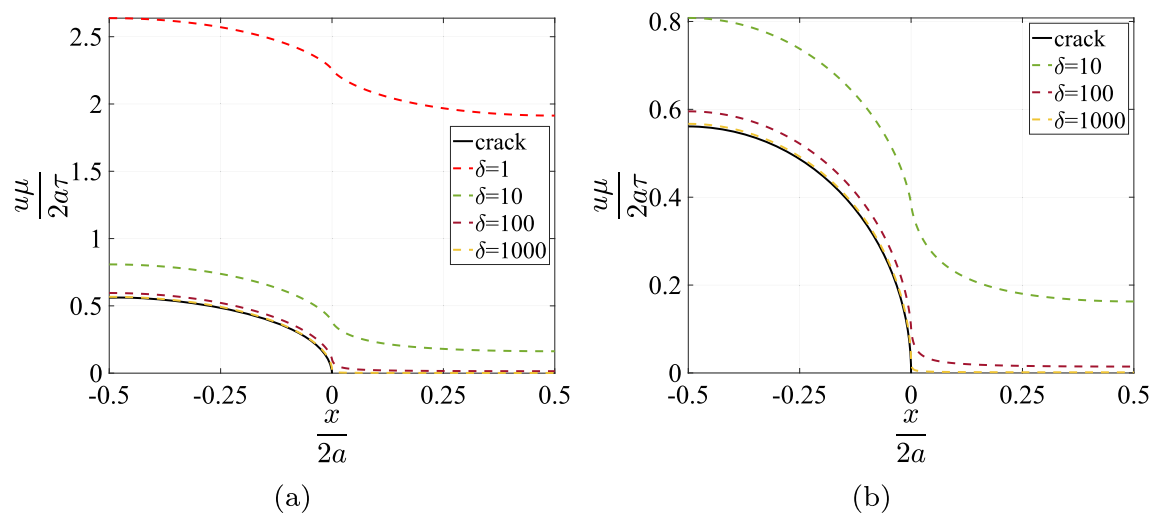
Fig. 19 The numerical solutions for the displacement along the interface, for increasing values of δ, converging to the analytic solution for a classical crack in an infinite homogeneous strip of finite width (A.8). The numerical solutions are obtained by the mesh type 1 with $N = 512$

Table 4 Improvement ratios I obtained using the singular elements in the uniform applied load problem

δ	Pattern\N	1	2	4	8	16	32	64	128	256
0.1	1	3.9	2.0	1.7	1.5	1.4	1.3	1.3	1.2	1.2
	2	6.5	3.1	2.2	1.8	1.6	1.5	1.4	1.4	1.3
	3	–	2.1	1.7	1.5	1.4	1.3	1.3	1.2	1.2
1	1	4.4	2.4	1.9	1.7	1.6	1.5	1.4	1.4	1.4
	2	6.7	3.2	2.3	1.9	1.7	1.6	1.5	1.4	1.4
	3	–	2.4	1.9	1.7	1.5	1.4	1.4	1.3	1.3
10	1	6.3	6.5	6.8	5.9	4.8	3.9	3.2	2.8	2.5
	2	4.9	3.5	2.8	2.3	2.1	1.9	1.8	1.7	1.6
	3	–	4.3	4.0	3.4	2.9	2.5	2.3	2.1	2.0
100	1	2.1	2.8	4.8	10.8	104.0	30.0	28.3	166.5	26.5
	2	1.9	2.1	2.5	2.7	2.7	2.4	2.1	2.0	1.9
	3	–	2.3	3.2	4.4	5.5	5.6	5.0	4.2	3.7
1000	1	1.2	1.3	1.5	1.8	2.4	3.8	7.7	36.3	26.1
	2	1.2	1.2	1.4	1.6	1.9	2.3	2.6	2.8	2.7
	3	–	1.2	1.4	1.6	2.0	2.8	4.1	5.6	6.5

the square root term $\sqrt{r}$ and only a very small part adjacent to the crack tip is governed by the $r \ln r$ term. The novel idea behind this proposal is to include in the singular element not only the most singular term in the problem to be solved, i.e. the term $r \ln r$ in the present case of a crack in spring interface, but also the most singular term in the limit problem for $\delta \to \infty$, i.e. the square root term $\sqrt{r}$, with the aim of covering well the whole range of δ values. The performance of such singular element will be studied in a forthcoming work.

Appendix A: Analytic solution for an infinite array of collinear identical cracks in an infinite plane under Mode III

Consider an infinite array of cracks of length $2a$ located on the x-axis in an infinite plane, with $2L > 2a$ being the distance between their centers, under antiplane shear produced by a remote uniform shear $\sigma_{yz} = \tau$.

By adapting the Westergaard approach [45] to this antiplane problem, and considering the origin of the Cartesian coordinates (x, y) in the center of one of these cracks, we can define the following Westergaard-type complex analytic function of $z = x + iy$, where $i = \sqrt{-1}$ is the imaginary unit,

$$Z'_{III}(z) = \frac{\tau \sin(\pi z/2L)}{\sqrt{\sin^2(\pi z/2L) - \sin^2(\pi a/2L)}}, \tag{A.1}$$

giving out-of-plane displacement $u = u_z = \frac{1}{\mu}\mathrm{Im}Z_{III}(z)$, and shear stresses $\sigma_{xz} = \mu u_{,x} = \mathrm{Im}Z'_{III}(z)$ and $\sigma_{yz} = \mu u_{,y} = \mathrm{Re}Z'_{III}(z)$.

From (A.1) we can deduce the SIF K_{III} for this array of cracks

$$K_{III} = \tau\sqrt{\pi a}\sqrt{\frac{2L}{\pi a}\tan\left(\frac{\pi a}{2L}\right)} = \tau\sqrt{2L\tan\left(\frac{\pi a}{2L}\right)}. \tag{A.2}$$

This leads to the ERR value

$$G_{III} = \frac{K_{III}^2}{2\mu} = \frac{\tau^2 L}{\mu}\tan\left(\frac{\pi a}{2L}\right), \tag{A.3}$$

which in the case $L = 2a$, studied in Sect. 5.3, gives

$$G_{III} = 2a\tau^2/\mu. \tag{A.4}$$

To get the variation of displacement $u(x, 0)$ along the upper crack face, for $-a < x < a$ and $y = 0$, we can just integrate the shear stress σ_{xz} as follows

$$-\frac{1}{\mu}\int_x^a \sigma_{xz}(x', 0)\mathrm{d}x' = -\int_x^a u_{,x'}(x', 0)\mathrm{d}x'$$

$$= u(x, 0) - u(a, 0) = u(x, 0), \tag{A.5}$$

considering that the crack tip displacement is zero. Hence,

$$u(x, 0) = \frac{\tau}{\mu}\int_x^a \frac{\sin(\pi x'/2L)}{\sqrt{\sin^2(\pi a/2L) - \sin^2(\pi x'/2L)}}\mathrm{d}x', \tag{A.6}$$

which can be evaluated analytically by some substitutions giving

$$u(x, 0) = \frac{2L\tau}{\pi\mu}\mathrm{ArcCoth}\frac{\cos(\pi x/2L)}{\sqrt{\cos^2(\pi x/2L) - \cos^2(\pi a/2L)}} \tag{A.7}$$

$$= \frac{L\tau}{\pi\mu}\ln\frac{\cos(\pi x/2L) + \sqrt{\cos^2(\pi x/2L) - \cos^2(\pi a/2L)}}{\cos(\pi x/2L) - \sqrt{\cos^2(\pi x/2L) - \cos^2(\pi a/2L)}}. \tag{A.8}$$

As explained in Sect. 5.1, taking into account that the symmetry planes in the middle between these cracks are free of shear stresses σ_{xz} the above solution is also valid for a one-crack problem in an infinitely long strip of width $2L$ with traction free lateral boundaries, analogous to those shown in Figs. 1 and 10b but with perfect interface instead of spring interface.

References

1. Winkler E (1867) Die Lehre von der Elastizität und Festigkeit mit besonderer Rücksicht auf ihre Anwendung in der Technik, für polytechnische Schulen, Bauakademien, Ingenieure, Maschienenbauer, Architecten, etc. Verlag von H. Dominicus, Prag
2. Dillard D, Mukherjee B, Karnal P, Batra R, Frechette J (2018) A review of Winkler's foundation and its profound influence on adhesion and soft matter applications. Soft Matter 14:3669–3683
3. Prandtl L (1933) A thought model for the fracture of brittle solids. Zeitschrift für Phys Angenwandte Math und Mech 13(2):129–133
4. Entov V, Salganik R (1968) On the Prandtl brittle fracture model. Mech Solids 3:79–89 (translated from Russian)
5. Lenci S (2001) Analysis of a crack at a weak interface. Int J Fract 108(3):275–290
6. Cornetti P, Mantič V, Carpinteri A (2012) Finite fracture mechanics at elastic interfaces. Int J Solids Struct 49:1022–1032
7. Cornetti P, Muñoz-Reja M, Mantic V (2022) Cohesive crack models and finite fracture mechanics analytical solutions for FRP-concrete single-lap shear test: an overview. Theor Appl Fract Mech 122:103529
8. Mantič V, Távara L, Blázquez A, Graciani E, París F (2015) A linear elastic - brittle interface model: Application for the onset and propagation of a fibre-matrix interface crack under biaxial transverse loads. Int J Fract 195:15–38
9. Muñoz-Reja M, Távara L, Mantič V (2018) Convergence of the BEM solution applied to the CCFFM for LEBIM. In: Key Engineering Materials, vol 774, Trans Tech Publ, pp 355–360
10. Távara L, Mantic V, Graciani E, Cañas J, París F (2010) Analysis of a crack in a thin adhesive layer between orthotropic materials:

an application to composite interlaminar fracture toughness test. Comput Model Eng Sci 58(3):247–270

11. Bialas M, Mróz Z (2005) Modelling of progressive interface failure under combined normal compression and shear stress. Int J Solids Struct 42(15):4436–4467

12. Valoroso N, Champaney L (2006) A damage-mechanics-based approach for modelling decohesion in adhesively bonded assemblies. Eng Fract Mech 73(18):2774–2801

13. Cornetti P, Sapora A, Carpinteri A (2016) Short cracks and V-notches: finite fracture mechanics vs. cohesive crack model. Eng Fract Mech 168:2–12

14. Dimitri R, Cornetti P, Mantič V, Trullo M, Lorenzis LD (2017) Mode-I debonding of a double cantilever beam: a comparison between cohesive crack modeling and finite fracture mechanics. Int J Solids Struct 124:57–72

15. Jiménez M, Cañas J, Mantič V, Ortiz J (2007) Numerical and experimental study of the interlaminar fracture test of composite-composite adhesively bonded joints. (in Spanish), Materiales Compuestos 07, Asociación Española de Materiales Compuestos, Universidad de Valladolid 499–506

16. Weißgraeber P, Becker W (2013) Finite fracture mechanics model for mixed mode fracture in adhesive joints. Int J Solids Struct 50:2383–2394

17. Muñoz Reja M, Távara L, Mantič V, Cornetti P (2016) Crack onset and propagation at fibre-matrix elastic interfaces under biaxial loading using finite fracture mechanics. Compos A 82:267–278

18. Muñoz Reja M, Cornetti P, Távara L, Mantič V (2020) Interface crack model using finite fracture mechanics applied to the double pull-push shear test. Int J Solids Struct, 188–189:56–73

19. Muñoz Reja M, Távara L, Mantič V, Cornetti P (2020) A numerical implementation of the coupled criterion of finite fracture mechanics for elastic interfaces. Theor Appl Fract Mech 108:102607

20. Costabel M, Dauge M (1996) A singularly perturbed mixed boundary value problem. Commun Partial Differ Equ 21(11–12):1919–1949

21. Sinclair GB (1999) A note on the removal of further breakdowns in classical solutions of Laplace's equation on sectorial regions. J Elast 56:247–252

22. Antipov Y, Avila-Pozos O, Kolaczkowski S, Movchan A (2001) Mathematical model of delamination cracks on imperfect interfaces. Int J Solids Struct 38(36):6665–6697

23. Mishuris G (2001) Interface crack and nonideal interface concept (Mode III). Int J Fract 107:279–296

24. Mishuris G, Kuhn G (2001) Asymptotic behaviour of the elastic solution near the tip of a crack situated at a nonideal interface. ZAMM - J Appl Math Mech/ Zeitschrift für Angewandte Mathematik und Mech 81(12):811–826

25. Jiménez-Alfaro S, Villalba V, Mantič V (2020) Singular elastic solutions in corners with spring boundary conditions under antiplane shear. Int J Fract 223(1):197–220

26. Jiménez-Alfaro S, Mantič V (2023) Crack tip solution for mode III cracks in spring interfaces. Eng Fract Mech 288:109293

27. Jiménez-Alfaro S, Mantič V (2020) FEM benchmark problems for cracks with spring boundary conditions under antiplane shear loadings. Aerotecnica Missili Spazio 99:309-319

28. Sinclair GB (1999) Logarithmic stress singularities resulting from various boundary conditions in angular corners of plates in extension. J Appl Mech 66:556–560

29. Helsing J, Jonsson A (2002) On the computation of stress fields on polygonal domains with v-notches. Int J Numer Methods Eng 53(2):433–453

30. Marin L, Lesnic D, Mantic V (2004) Treatment of singularities in Helmholtz-type equations using the boundary element method. J Sound Vib 278(1):39–62

31. Barsoum RS (1974) Application of quadratic isoparametric finite elements in linear fracture mechanics. Int J Fract 10:603–605

32. Henshell RD, Shaw KG (1975) Crack tip finite elements are unnecessary. Int J Numer Methods Eng 9:495–507

33. Barsoum RS (1976) On the use of isoparametric finite elements in linear fracture mechanics. Int J Numer Methods Eng 10(1):25–37

34. Hussain MA, Lorensen WE, Pflegel G (1976) The quarter-point quadratic isoparametric element as a singular element for crack problems. In: Nastran user's experience, NASA TM-X-3428. pp 419–438

35. Banks-Sills L (1987) Quarter-point singular elements revisited. Int J Fract 34:R63–R69

36. París F, Cañas J (1997) Boundary element method, fundamentals and applications. Oxford University Press, Oxford

37. Medková D (2018) The Laplace equation. Boundary value problems on bounded and unbounded Lipschitz domains, Springer, Cham

38. Sayas FJ, Brown TS, Hassell ME (2019) Variational techniques for elliptic partial differential equations. Theoretical tools and advanced applications. CRC Press

39. Zienkiewicz O, Zhu J (1992) The superconvergent patch recovery and a posteriori error estimates. Part 1: the recovery technique. Int J Numer Meth Eng 33:1331–1364

40. Hughes TJ, Akin J (1980) Techniques for developing 'special' finite element shape functions with particular reference to singularities. Int J Numer Meth Eng 15(5):733–751

41. Wolfram S (1991) Mathematica: a system for doing mathematics by computer. Addison-Wesley, Redwood City

42. Alberty J, Carstensen C, Funken SA (1999) Remarks around 50 lines of Matlab: short finite element implementation. Numer Algorithms 20(2):117–137

43. Costabel M, Dauge M, Suri M (1998) Numerical approximation of a singularly perturbed contact problem. Comput Methods Appl Mech Eng 157(3):349–363

44. Jiménez-Alfaro S (2020) Singular elastic solutions for corners and cracks with spring boundary conditions, Master thesis, University of Seville

45. Westergaard HM (1939) Bearing pressures and cracks. J Appl Mech 6:49–53